Dalton Transactions

ROYAL SOCIETY OF CHEMISTRY

PAPER

View Article Online
View Journal

Cite this: DOI: 10.1039/d6dt00428h

Xanthene-anchored salen-based open and closed dinuclear indium complexes: synthesis and photophysical properties

Yoseph Kim,†[a,b] Ji Hye Lee, †[c] Hyeongkwon Moon,[b] Himchan Mo,[d] Hyonseok Hwang, [c] Junseong Lee, [d] Jun Hui Park, [b] Youngjo Kim *[b] and Myung Hwan Park *[a]

Xanthene-anchored dinuclear salen-based indium complexes with well-defined open and closed topologies were designed to elucidate how dinuclear geometry governs excited-state decay processes in indium luminophores. A rigid yet non-planar xanthene linker enables controlled formation of open (**XPOIn** and **XNOIn**) and closed (**XPCIn** and **XNCIn**) dinuclear architectures *via* a one-pot synthetic protocol. Single-crystal X-ray diffraction analyses of **XNOIn** and **XNCIn** revealed distinct spatial arrangements of the two salen–indium units, accompanied by different degrees of intramolecular π–π interactions and conformational rigidity. All complexes exhibited strong visible absorption bands originating from salen-centered π–π* transitions with partial charge-transfer (CT) characteristics and displayed yellow fluorescence in both solution and solid states. Notably, the open dinuclear systems consistently exhibited higher PLQYs than their closed analogues, despite the latter exhibiting more stabilised frontier molecular orbitals. Photophysical analysis revealed that the enhanced emission efficiency of the open systems originated from the increased radiative decay rates and suppressed non-radiative relaxation pathways. These results demonstrate that dinuclear topology plays a key role in governing excited-state dynamics in salen–indium systems and provide a useful framework for the rational design of multinuclear indium-based luminophores.

Received 18th February 2026,
Accepted 14th March 2026

DOI: 10.1039/d6dt00428h

rsc.li/dalton

Introduction

Indium-based coordination complexes have attracted increasing interest owing to the intrinsic stability and electronic characteristics of indium, a Group 13 element.[1–4] However, in contrast to boron-, aluminum-, and gallium-based luminophores,[5–17] luminescent indium complexes remain relatively underexplored, particularly with respect to achieving high photoluminescence efficiencies. This lack of research attention is often attributed to the relatively high atomic mass of indium and its associated electronic structure, which can facilitate non-radiative decay pathways and diminish the emission efficiency.[2,4,18]

A widely adopted strategy to overcome these limitations involves the use of a ligand-centered design, in which rigid and π-conjugated frameworks suppress vibrational relaxation and promote radiative decay. Among the various ligand platforms, salen-based N_2O_2 chelates have proven effective for various metal-based luminophores,[19–23] and particularly for indium fluorophores,[24–26] as they provide a robust coordination environment and enable fine electronic modulation through substituent effects. Consequently, numerous mononuclear salen–indium complexes exhibiting tunable emission colors and improved quantum yields have been reported.[27–30] However, these systems are largely limited to mononuclear architectures, inherently restricting the structural and photophysical diversity of salen–indium chemistry.

Dinuclear metal complexes offer an attractive yet underexplored opportunity to introduce additional degrees of freedom, such as interchromophoric interactions, geometric constraints, and topology-dependent excited-state dynamics, into the design of luminophores. Although a few dimeric indium complexes based on quinolinolate ligands, primarily arising from thermodynamic aggregation rather than intentional design, have been previously reported,[31] systematic

[a]Department of Chemistry Education, Chungbuk National University, Chungbuk 28644, Republic of Korea. E-mail: mhpark98@chungbuk.ac.kr
[b]Department of Chemistry, Chungbuk National University, Chungbuk 24341, Republic of Korea. E-mail: ykim@chungbuk.ac.kr, jhp@chungbuk.ac.kr
[c]Department of Chemistry and Institute for Molecular Science and Fusion Technology, Kangwon National University, Gangwon 24341, Republic of Korea
[d]Department of Chemistry, Chonnam National University, Gwangju 61186, Republic of Korea
† These authors contributed equally to this work.

studies on structurally defined dinuclear indium luminophores, particularly those based on salen ligands, remain scarce. Consequently, the influence of dinuclear topology on the photophysical behavior of indium complexes has yet to be clarified.

Meanwhile, Pacman ligands bearing benzofuran or xanthene spacers are well-established platforms for constructing dinuclear metal complexes and can be used to maintain two metal centers in a face-to-face arrangement within an appropriate topology.[32,33] Herein, we report a series of xanthene-anchored, salen-based dinuclear indium complexes with well-defined open and closed geometries. We used a xanthene linker because it provides a rigid yet nonplanar scaffold that allows controlled modulation of the intersalen orientation without altering the primary coordination environment of the indium centers.[34,35] By directly comparing open and closed dinuclear topologies, we aim to address the fundamental question of how dinuclear geometry governs radiative and non-radiative decay processes in salen–indium luminophores. Through combined structural, photophysical, electrochemical, and theoretical analyses, we demonstrate that dinuclear topology plays a key role in determining emission efficiency, beyond simple considerations of π-conjugation or orbital stabilization.

Results and discussion

Synthesis and characterization

The optimized synthetic routes for salen-based open (**XPOIn** and **XNOIn**) and closed (**XPCIn** and **XNCIn**) dinuclear indium complexes anchored by a xanthene group are presented in Scheme 1. All complexes were readily synthesized and obtained in high yields (45–70%) using a one-pot synthetic reaction[27] of **1**, $InMe_3$, and the respective amines in refluxing EtOH. Similar to mononuclear indium complexes, all dinuclear complexes also exhibited good solubility in common organic solvents, such as toluene, THF, and CH_2Cl_2. The formation of complexes was confirmed by ^1H and ^{13}C NMR spectroscopy (Fig. S1–S4 in the SI) and elemental analysis. The ^1H and ^{13}C NMR spectra of the obtained open (**XPOIn** and **XNOIn**) and closed (**XPCIn** and **XNCIn**) dinuclear indium complexes showed the expected resonances corresponding to xanthene moieties and the specific In–CH_3 protons at around −0.5 ppm. The integral value of the dimethyl protons of the xanthene group in both **XPCIn** and **XNCIn** was twice that in **XPOIn** and **XNOIn**. The ^1H NMR spectra of all four complexes show a single set of well-defined resonances consistent with a predominant symmetric species on the NMR timescale. Although minor conformational equilibria cannot be fully excluded, the obtained NMR spectra indicate that a single dominant conformer is present in solution under the conditions studied.

The crystal structures of **XNOIn** and **XNCIn** were further characterized by X-ray crystallographic studies, confirming the open and closed structures of **XNOIn** and **XNCIn**, respectively, (Fig. 1 and Tables S1–S4 in the SI). The geometry around the indium centres of the two complexes is slightly distorted square-pyramidal, as determined using the trigonality parameters[36] (0.11–0.29). In both structures, the indium centers are oriented outward. However, the two complexes exhibit slightly different geometries for the xanthene unit. In the open structure of **XNOIn**, the two benzene rings of the xanthene unit were bent by approximately 25°. In contrast, in the closed form of **XNCIn**, one xanthene fragment adopted an anthracene-like, nearly planar conformation, whereas the other one was more distorted with two benzene rings bent by approximately 36°. Each complex contained two salen moieties, which exhibited noticeable π–π interactions. In addition, the dihedral angles (C(Ph)–C═N–C(Naph)) in the open form were 176.20°, 175.62°, 175.43°, and 168.41°, which were comparable to those in the closed form (178.12°, 177.14°, 174.95°, and 173.37°). These values fall within a narrow range, indicating that macrocyclization does not introduce significant distortion in the primary coordination environment. Although the two naphthalene rings were not perfectly parallel, the shortest distances between the closest carbon atom and the adjacent naphthalene ring were 3.28 Å in **XNOIn** and 3.16 Å in **XNCIn**, within the typical range for π–π interactions.

Optical and electrochemical analyses for indium complexes

To investigate the optical properties of all dinuclear indium complexes, UV–vis absorption and photoluminescence (PL) spectra were recorded in deoxygenated toluene (20 μM) at room temperature (Fig. 2 and Table 1). Both open (**XPOIn** and **XNOIn**) and closed (**XPCIn** and **XNCIn**) complexes exhibited two intense major absorption bands. The strong absorption

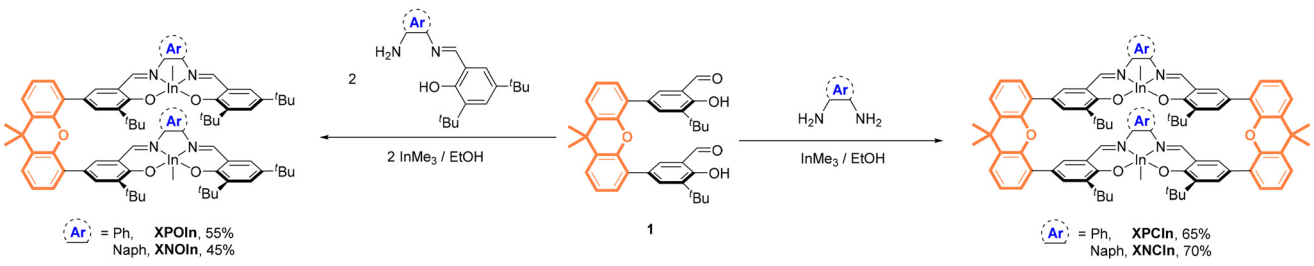

Scheme 1 Synthetic routes for salen-based open (**XPOIn** and **XNOIn**) and closed (**XPCIn** and **XNCIn**) dinuclear indium complexes anchored by xanthene.

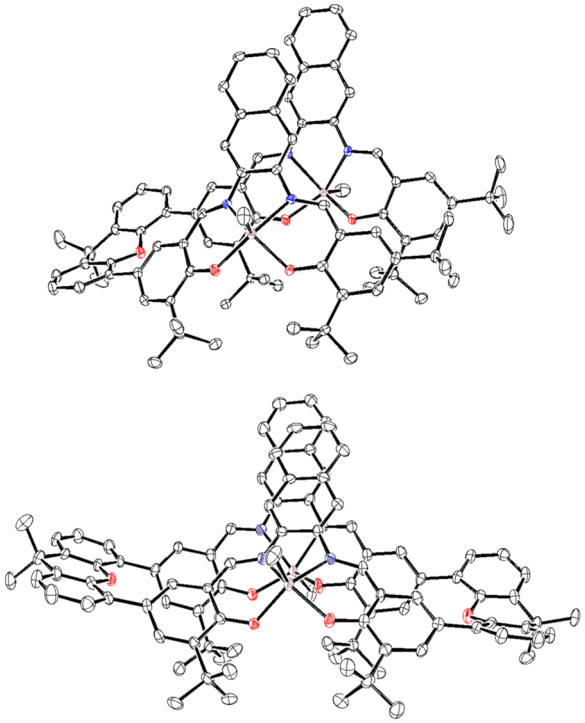

Fig. 1 X-ray crystal structures of **XNOIn** (top) and **XNCIn** (bottom) (50% thermal ellipsoids): H atoms are omitted for clarity.

band observed at 308–313 nm was attributed to the locally excited transition of the xanthene moiety.[34] The moderately strong band at 435–450 nm was assigned to the typical salen-centered π–π* transition, which has also been reported in previous mononuclear salen–indium complexes.[28–30] In addition, the low-energy absorption bands of **XNOIn** and **XNCIn** were slightly blue-shifted ($\Delta\lambda_{abs}$ = 2 nm for **XNOIn** and $\Delta\lambda_{abs}$ = 5 nm for **XNCIn**) with an increase in solvent polarity (toluene < THF), indicating partial charge-transfer (CT) characteristics (Fig. S5 and Table S5 in the SI). In contrast, the low-energy bands of the closed complexes **XPCIn** and **XNCIn** were slightly red-shifted compared to those of the open complexes **XPOIn** and **XNOIn**. This red-shift originates from altered relative orientation and enhanced electronic communication between the two salen units within the constrained macrocyclic topology in the closed complexes (see the "Theoretical calculations and orbital analysis" section). Meanwhile, the molar absorption coefficients (ε) of the closed complexes (**XPCIn** and **XNCIn**) with two xanthene groups were found to be larger than those of the open complexes (**XPOIn** and **XNOIn**) with one xanthene group. Interestingly, naphthylene-based complexes exhibited larger ε values than their phenylene-based counterparts, likely reflecting specific electronic interactions unique to each structure.

Electrochemical studies using cyclic voltammetry (CV) indicate that dinuclear indium complexes (**XPCIn**, **XNCIn**, **XPOIn**, and **XNOIn**) underwent irreversible oxidation (Fig. S6 in the SI). The oxidation onset potentials (E_{ox}) of **XPCIn** (E_{ox} = 0.37 V)

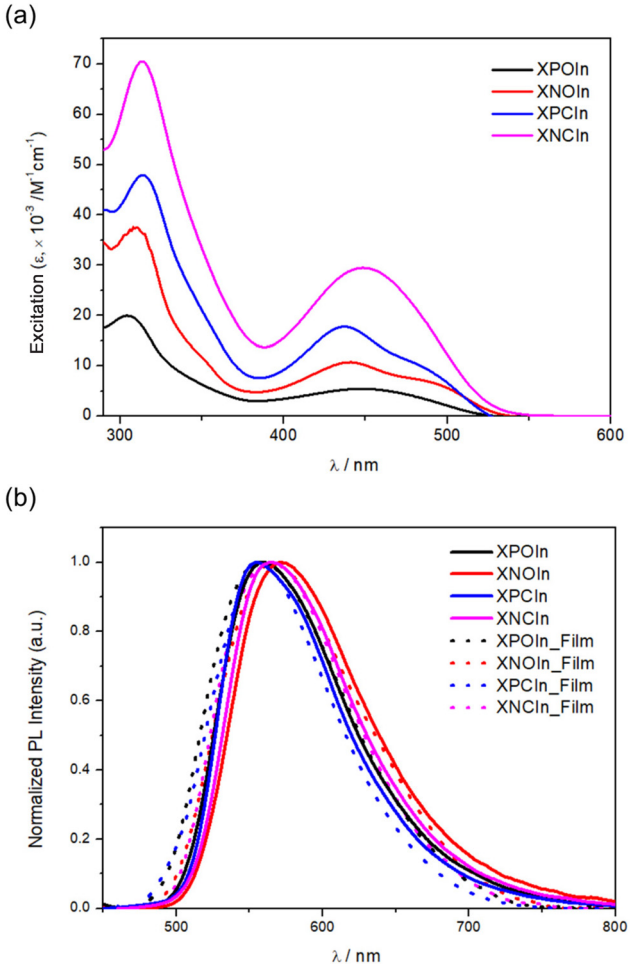

Fig. 2 (a) UV–vis absorption and (b) PL spectra (solid lines in toluene (20 μM) and dotted lines in the film state (5 wt% in PMMA)) of open (**XPOIn** and **XNOIn**) and closed (**XPCIn** and **XNCIn**) dinuclear indium complexes at 298 K.

and **XNCIn** (E_{ox} = 0.37 V) were anodically shifted compared with those of **XPOIn** (E_{ox} = 0.29 V) and **XNOIn** (E_{ox} = 0.21 V), respectively. The observed E_{ox} values indicate that the HOMO energy levels (−5.17 eV) of **XPCIn** and **XNCIn** are slightly lower than those of **XPOIn** (−5.09 eV) and **XNOIn** (−5.01 eV). Additionally, the LUMO energy levels, calculated using the optical band gaps and HOMO energy levels, for **XPCIn** (−2.83 eV) and **XNCIn** (−2.84 eV) are more stabilized than those of **XPOIn** (−2.70 eV) and **XNOIn** (−2.60 eV). These results support macrocycle-induced orbital redistribution and enhanced electronic coupling between the two salen units within the constrained framework of the closed dinuclear systems.

The PL spectra of dinuclear indium complexes exhibit yellow emissions centered at 556–574 nm and broad emission patterns in toluene solutions at 298 K (Fig. 2 and Table 1), assigned to the typical π–π* electronic transitions based on the entire salen framework, including the xanthene anchor (see the "Theoretical calculations and orbital analysis" section). This feature is analogous to that reported for previously

Table 1 Photophysical data of open and closed dinuclear indium complexes

Compd	λ_{abs} [a]/nm ($\varepsilon \times 10^{-3}$ M^{-1} cm^{-1})	λ_{ex} [a]/nm	λ_{em}/nm		Φ_{PL} [c]/%		τ [d]/ns		k_r [e]/$\times 10^7$ s^{-1}		k_{nr} [f]/$\times 10^8$ s^{-1}		HOMO/LUMO [g]/eV
			Tol[a]	Film[b]	Tol[a]	Film[b]	Tol[a]	Film[b]	Tol[a]	Film[b]	Tol[a]	Film[b]	
XPOIn	309 (19.41), 435 (5.18)	431	557	558	9.2	18.1	0.52	1.18	17.7	15.4	17.5	6.9	−5.09/−2.70
XNOIn	308 (36.23), 446 (10.56)	443	574	567	10.3	25.4	0.59	1.22	17.5	20.8	15.2	6.1	−5.01/−2.60
XPCIn	310 (47.12), 440 (17.56)	436	556	554	5.5	11.7	0.69	0.96	8.0	12.1	13.7	9.2	−5.17/−2.83
XNCIn	313 (70.47), 452 (29.46)	453	563	564	8.0	14.5	0.67	1.13	11.9	12.8	13.7	7.6	−5.17/−2.84

[a] In deoxygenated toluene at 298 K (20 μM). [b] In spin-coated PMMA film doped with the compound at 5 wt%. [c] Absolute photoluminescence quantum yield (PLQY). [d] Emission lifetime. [e] $k_r = \Phi_{PL}/\tau$. [f] $k_{nr} = k_r(1/\Phi_{PL} - 1)$. [g] Calculated from electrochemical E_{ox} with reference to ferrocene/ferrocenium (Fc/Fc^+).

observed mononuclear salen-based indium complexes.[18] Although no significant differences are observed in the emission maxima (λ_{em}) between open dinuclear complexes (**XPOIn** and **XNOIn**) and closed dinuclear complexes (**XPCIn** and **XNCIn**), the λ_{em} values of the closed systems are slightly blue-shifted compared to those of the corresponding open systems. A similar trend is observed for the film state. The emission spectra of **XNOIn** and **XNCIn** in THF are similar to those observed in toluene (Fig. S5 and Table S5 in the SI), consistent with their low-energy absorption profiles. Additionally, both complexes exhibit a rigidochromic blue shift in the rigid state of THF at 77 K (Fig. S5 and Table S5 in the SI). The single-exponential PL decay lifetimes (τ) of all complexes, measured in both solution and film states, are in the nanosecond range, indicating a fluorescent nature (Table 1 and Fig. S7–S10 in the SI).

The absolute PLQYs (Φ_{PL}) of all dinuclear indium complexes were measured in deoxygenated toluene and in the PMMA film state (Table 1). The PLQYs in toluene (5–10%) are lower than those in the film state (12–25%). Interestingly, the PLQYs of the open complexes **XPOIn** and **XNOIn** were higher than those of the closed complexes **XPCIn** and **XNCIn** both in toluene and in the film state. This finding can be elucidated by comparing the radiative decay constant (k_r) and non-radiative constant (k_{nr}) in both the open and closed systems. In particular, in the film state, the k_r values of open dinuclear **XPOIn** ($k_r = 15.4 \times 10^7$ s^{-1}) and **XNOIn** ($k_r = 20.8 \times 10^7$ s^{-1}) are higher than those of closed dinuclear **XPCIn** ($k_r = 12.1 \times 10^7$ s^{-1}) and **XNCIn** ($k_r = 12.8 \times 10^7$ s^{-1}), respectively, while the k_{nr} values of the open dinuclear complexes ($<7.0 \times 10^8$ s^{-1}) are relatively lower than those of the closed dinuclear systems ($>7.5 \times 10^8$ s^{-1}).

To determine the aggregation effect of the open and closed dinuclear indium systems with the xanthene anchor, additional PL measurements for both **XNOIn** and **XNCIn** were performed in the solid state and in THF/water solutions with different fractions (Fig. 3 and Table S5 in the SI). Although a slight rigidochromic red shift was observed in the solid state compared to that in the toluene and THF solutions, the overall emission profiles remained consistent with those in the solutions. Additionally, the PLQYs of **XNOIn** and **XNCIn** were found to be 24.8% and 16.0%, respectively, which were similar to those in each film and the rigid state (THF at 77 K, Table S5 in the SI). In the THF/water mixture, only the overall intensity of the emission bands for both **XNOIn** and **XNCIn** gradually decreased without any change in λ_{em} with an increase in water fraction (f_w). No intermolecular emission bands resulting from aggregation or molecular packing were observed. This behaviour is attributed to the slightly staggered arrangement of the two salen-based indium moieties induced by the bent xanthene unit.

Theoretical calculations and orbital analysis

To gain insights into the nature of the electronic transitions of the xanthene-anchored open and closed dinuclear indium complexes, theoretical calculations were performed on the ground-state (S_0)-optimized structures of the complexes using time-dependent density functional theory (TD-DFT) at the B3LYP/6-31G(d,p) level (Fig. 4 and Fig. S11–S14, Tables S6–S17 in the SI). The major low-energy absorptions ($f_{calc} > 0.05$) of **XPOIn**, **XNOIn**, **XPCIn**, and **XNCIn** in the S_0 state were mainly related to the electronic transitions from the HOMO (>85%) or HOMO−2 (>80%), where the electronic contributions were distributed over the xanthene-linked phenoxy moieties, to the LUMO (>99%) or LUMO+2 (>99%), where the contributions were localized on the aryl-bridged phenoxy imine moieties. These absorptions corresponded to the salen-centered π–π* transitions involving partial CT characteristics. Interestingly, the xanthene groups had an electronic contribution of 12–26% to only the HOMO or HOMO−2. Notably, their contribution in the closed systems (23–26%) is slightly larger than that in the open systems (12–19%). Furthermore, the calculated low-energy absorption wavelengths of the open dinuclear complexes (**XPOIn** and **XNOIn**) are lower than those of the corresponding closed dinuclear complexes (**XPCIn** and **XNCIn**). These results are in good agreement with the experimental photophysical data.

Experimental

General considerations

All experimental manipulations were performed under an inert N_2 atmosphere using standard Schlenk and glove box

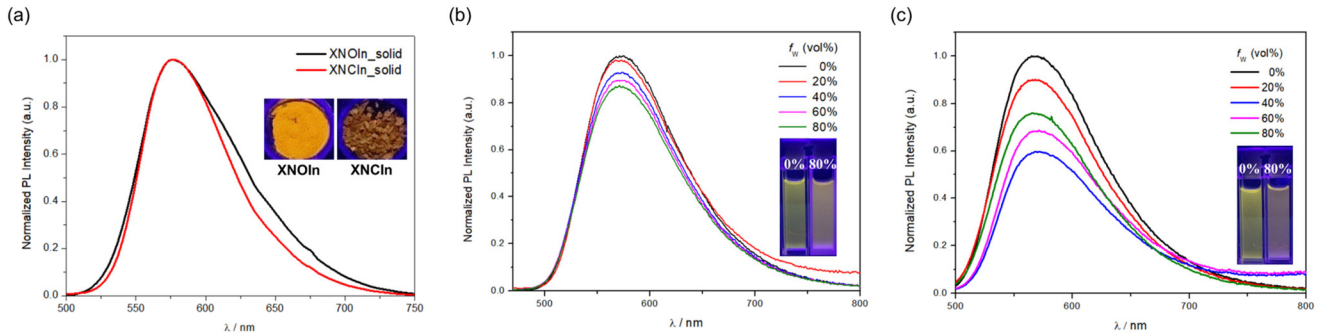

Fig. 3 (a) PL spectra of **XNOIn** (λ_{ex} = 443 nm) and **XNCIn** (λ_{ex} = 453 nm) in a neat solid state at 298 K. Inset: emission images taken using a hand-held UV lamp (λ_{ex} = 365 nm). PL spectra of (b) **XNOIn** (λ_{ex} = 443 nm) and (c) **XNCIn** (λ_{ex} = 453 nm) in THF/water mixtures (20 μM) and the emission color of the 0% and 80% water mixture under a hand-held UV lamp (λ_{ex} = 365 nm).

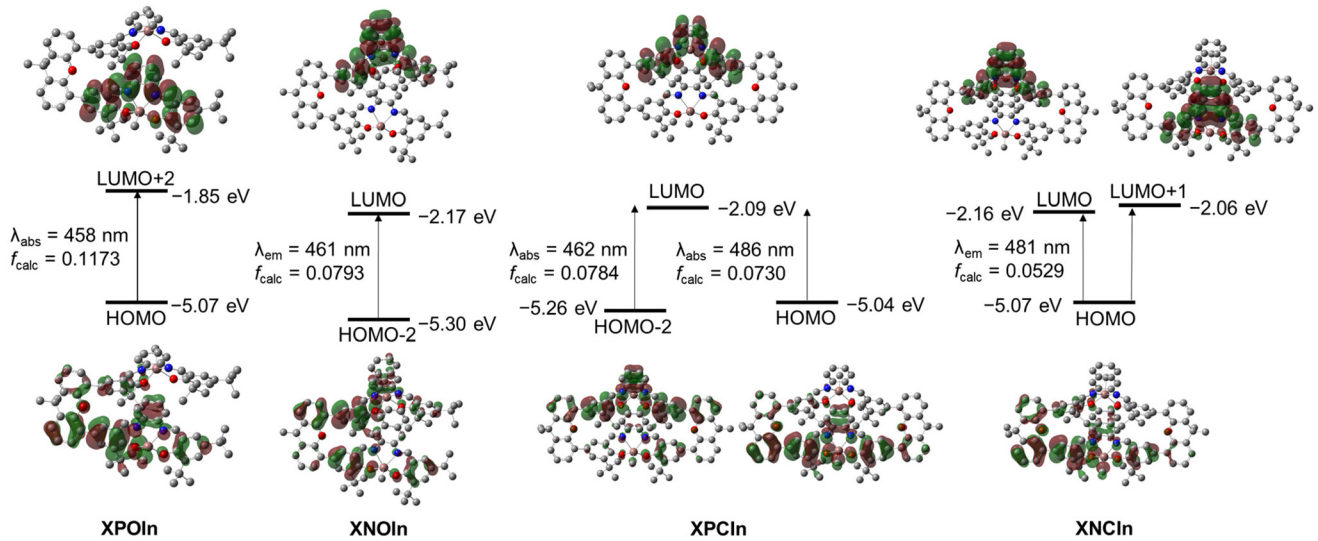

Fig. 4 Frontier molecular orbitals (MOs) of **XPOIn**, **XNOIn**, **XPCIn**, and **XNCIn** in their S_0-states with their relative energies from DFT calculations (isovalue = 0.04). The transition energy (in nm) was calculated using the TD-B3LYP method at the 6-31G(d, p) level.

techniques. All commercially available reagents were purchased from Sigma-Aldrich and used without further purification. All anhydrous grade solvents (tetrahydrofuran (THF), ethanol (EtOH), and toluene) purchased from Alfa Aesar were dried by passing them *via* an activated alumina column and stored over activated molecular sieves (5 Å). Spectrophotometric grade solvents (toluene and tetrahydrofuran (THF)) were used without further purification. Compounds **1**,[37] 2-[(2-amino-phenylimino)-methyl]-4,6-di-*tert*-butylphenol,[38] 2-[((3-amino-2-naphthalenyl)imino)methyl]-4,6-di-*tert*-butylphenol,[39] and trimethylindium ($InMe_3$)[12] were prepared according to previously reported literature procedures. $InMe_3$ is a highly pyrophoric compound and should be handled under an inert atmosphere and stored in a glovebox to ensure safe manipulation. Deuterated solvent ($CDCl_3$ (chloroform-d_1)) from Cambridge Isotope Laboratories was used after further drying over activated molecular sieves (5 Å). NMR spectra were recorded using a Bruker Avance 500 spectrometer at ambient temperature. The chemical shifts were recorded in ppm and referenced against external Me_4Si (^1H and ^{13}C).[40] Elemental analyses were performed using an EA3000 (Eurovector). Cyclic voltammetry experiments were performed using a potentiostat (CH Instruments).

Synthesis of XPOIn

A reaction mixture comprising **1** (0.28 g, 0.5 mmol) and 2-[(2-amino-phenylimino)-methyl]-4,6-di-*tert*-butylphenol (0.32 g, 1.0 mmol) was dissolved in EtOH (10 mL) and stirred at room temperature for 1 h. Then, $InMe_3$ (0.17 g, 1.1 mmol) dissolved in EtOH (10 mL) was added to the reaction mixture and refluxed for 12 h. After cooling to room temperature, the resulting mixture was filtered. The filtrate was collected and all volatiles were removed under reduced pressure. The residue was washed with cold EtOH (20 mL) and dried *in vacuo* to obtain **XPOIn** as a bright yellow solid (0.39 g, 55% yield). ^1H NMR ($CDCl_3$, 500.13 MHz): δ 8.45 (s, 2H), 8.11 (s, 2H), 7.69 (d, J =

2.3 Hz, 2H), 7.43 (d, J = 8.3 Hz, 2H) 7.40 (s, 4H), 7.38 (d, J = 1.4 Hz, 2H), 7.31 (d, J = 7.8 Hz, 2H), 7.25 (d, J = 1.5 Hz, 1H), 7.23 (d, J = 1.5 Hz, 1H), 7.12 (m, 6H), 6.86 (d, J = 2.0 Hz, 2H), 1.78 (s, 3H), 1.72 (s, 3H), 1.37 (s, 18H), 1.31 (s, 18H), 1.27 (s, 18H), −0.60 (s, 6H, In–CH_3). ^{13}C NMR ($CDCl_3$, 125.76 MHz): δ 170.94, 170.90, 169.58, 169.54, 163.92, 147.04, 142.79, 142.67, 138.99, 136.38, 134.84, 134.80, 130.85, 130.33, 129.23, 129.21, 128.78, 127.70, 127.56, 124.53, 124.11, 123.07, 118.83, 118.54, 116.94, 116.24, 35.51, 35.35, 34.27, 33.86, 31.34, 31.28, 29.52, 29.45, 29.37. Anal. calcd for $C_{81}H_{94}In_2N_4O_5$: C, 67.96; H, 6.48; N, 3.91. Found: C, 65.87; H, 6.72; N, 3.81.

Synthesis of XNOIn

This complex was synthesized in a manner analogous to the synthesis of **XPOIn** using 2-[((3-amino-2-naphthalenyl)imino) methyl]-4,6-di-*tert*-butylphenol (0.37 g, 1.0 mmol). The desired **XNOIn** was obtained as a bright yellow solid (0.34 g, 45% yield). ^{1}H NMR ($CDCl_3$, 500.13 MHz): δ 8.45 (s, 2H), 7.68 (d, J = 2.2 Hz, 2H), 7.38 (m, 13H), 7.31 (d, J = 8.0 Hz, 2H), 7.25 (m, 3H), 7.23 (d, J = 1.5 Hz, 1H), 7.10 (m, 5H), 6.86 (d, J = 2.0 Hz, 2H), 1.78 (s, 3H), 1.72 (s, 3H), 1.37 (s, 18H), 1.31 (s, 18H), 1.27 (s, 18H), −0.60 (s, 6H, In–CH_3). ^{13}C NMR ($CDCl_3$, 125.76 MHz): δ 171.00, 169.89, 165.39, 165.33, 160.03, 147.60, 142.60, 139.23, 138.87, 137.87, 136.38, 132.97, 132.59, 131.11, 130.67, 129.21, 128.63, 128.29, 127.90, 127.43, 126.71, 126.68, 125.20, 124.13, 123.35, 123.24, 120.09, 118.45, 114.71, 114.65, 35.63, 35.36, 34.69, 34.55, 33.97, 31.36, 29.63, 29.57, 29.09. Anal. calcd for $C_{89}H_{96}In_2N_4O_5$: C, 69.80; H, 6.32; N, 3.66. Found: C, 67.02; H, 6.07; N, 3.52.

Synthesis of XPCIn

A reaction mixture comprising **1** (0.28 g, 0.50 mmol) and 1,2-phenylenediamine (0.054 g, 0.50 mmol) was dissolved in EtOH (15 mL) and refluxed for 1 h. Then, $InMe_3$ (0.09 g, 0.55 mmol) dissolved in EtOH (10 mL) was added to the reaction mixture and refluxed for 12 h. After cooling to room temperature, the resulting mixture was filtered. The filtrate was collected, and all volatiles were removed under reduced pressure. The residue was washed with cold EtOH (20 mL) and dried *in vacuo* to obtain **XPCIn** as an orange solid (0.25 g, 65% yield). ^{1}H NMR ($CDCl_3$, 500.13 MHz): δ 7.99 (s, 4H), 7.68 (d, J = 2.3 Hz, 4H), 7.42 (d, J = 1.6 Hz, 2H), 7.40 (d, J = 1.6 Hz, 2H), 7.36 (d, J = 2.3 Hz, 4H), 7.29 (dd, J_1 = 5.9 Hz, J_2 = 3.5 Hz, 4H), 7.27 (d, J = 1.6 Hz, 2H), 7.25 (d, J = 1.5 Hz, 2H), 7.18 (s, 1H), 7.16 (s, 2H), 7.14 (s, 1H), 6.91 (m, 4H), 1.86 (s, 6H), 1.65 (s, 6H), 1.31 (s, 36H), −0.48 (s, 6H, In–CH_3). ^{13}C NMR ($CDCl_3$, 125.76 MHz): δ 170.91, 163.64, 147.24, 143.07, 138.85, 134.92, 133.67, 130.48, 129.34, 129.07, 127.38, 124.28, 123.98, 123.08, 118.89, 116.40, 35.37, 35.07, 34.38, 30.36, 29.30. Anal. calcd for $C_{88}H_{86}In_2N_4O_6$: C, 69.30; H, 5.68; N, 3.67. Found: C, 68.24; H, 5.52; N, 3.55.

Synthesis of XNCIn

This complex was synthesized in a manner analogous to that for **XPCIn** using 2,3-diaminonaphthalene (0.079 g, 0.50 mmol). The desired **XNCIn** was obtained as an orange solid (0.28 g, 70% yield). ^{1}H NMR ($CDCl_3$, 500.13 MHz): δ 8.08 (s, 4H), 7.75 (d, J = 2.3 Hz, 4H), 7.51 (d, J = 2.3 Hz, 6H), 7.47 (s, 4H), 7.43 (d, J = 1.6 Hz, 2H), 7.42 (d, J = 1.5 Hz, 2H), 7.33 (d, J = 1.5 Hz, 2H), 7.32 (d, J = 1.5 Hz, 2H), 7.20 (s, 2H), 7.18 (s, 2H), 7.17 (s, 2H), 6.89 (m, 4H), 1.89 (s, 6H), 1.68 (s, 6H), 1.34 (s, 36H), −0.54 (s, 6H, In–CH_3). ^{13}C NMR ($CDCl_3$, 125.76 MHz): δ 171.12, 164.24, 147.27, 143.21, 137.70, 134.95, 133.81, 131.88, 130.57, 129.27, 129.05, 127.39, 126.29, 124.38, 124.04, 123.15, 119.22, 114.15, 35.42, 35.14, 34.43, 30.51, 29.36. Anal. calcd for $C_{96}H_{90}In_2N_4O_6$: C, 70.94; H, 5.58; N, 3.45. Found: C, 68.32; H, 5.50; N, 3.36.

X-ray crystallography

Single crystals of **XNOIn** and **XNCIn** were obtained from $CHCl_3$/*n*-hexane mixed solutions. The crystals used for X-ray diffraction analysis were coated with paratone oil and mounted on glass capillaries. Crystallographic measurements were taken using a Bruker APEX II CCD detector diffractometer with graphite monochromated Mo-Kα radiation (λ = 0.71073 Å) at 100 K. The solid-state structures were solved using direct methods and all non-hydrogen atoms underwent anisotropic refinement using a full-matrix least-squares method on F^2 using the SHELXTL/PC package to obtain data in the CIF format (CCDC 2530423 for **XNOIn** and 2530424 for **XNCIn**). Hydrogen (H) atoms were placed at their geometrically calculated positions and refined by placing them on the corresponding carbon (C) atoms using isotropic thermal parameters. Detailed crystallographic data for the two complexes and selected bond lengths and angles are provided in Tables S1–S4 of the SI.

Optical and electrochemical measurements

UV/vis absorption and PL spectra were recorded using Cary 8454 (Agilent) and FluoroMax Plus (HORIBA) spectrophotometers, respectively. Solution PL spectra were recorded in deoxygenated solutions (20 μM in toluene and THF). Deoxygenated solvents were prepared by degassing spectroscopic grade solvents for ∼30 min and storing them in a nitrogen-filled glove box. The PL spectra and PLQYs of the films were obtained using poly(methyl methacrylate) (PMMA) matrices doped with the compounds (5 wt% *vs.* PMMA on quartz plates). The absolute PLQYs of the solution, film, and solid samples were measured using a FluoroMax Plus spectrophotometer (HORIBA) equipped with a 3.2-inch integrating sphere (FL-QM, HORIBA). The PL decay was measured using a FluoroMax Plus spectrophotometer equipped with a DeltaTime time-correlated single-photon counting (TCSPC) kit. The PL decay lifetimes were estimated by fitting the decay curves measured in the TCSPC mode. CV measurements were performed using a 760E potentiostat (CH Instruments) in MeCN containing 1 mM electroactive species and 100 mM $TBAPF_6$ as the supporting electrolyte. The measurements were performed using three-electrode cells inside a Faraday cage at room temperature. A Pt disk (diameter: 3 mm) was used as the working electrode, while $Ag/AgNO_3$ (10 mM in MeCN) and a Pt wire were used as the counter and reference electrodes, respectively.

Prior to the measurements, all electrolyte solutions were sparged with Ar for 30 minutes to remove O_2. The oxidation potential of all complexes was recorded at a scan rate of 100 mV s^{-1} and was determined relative to a ferrocene/ferrocenium (Fc/Fc^+) redox couple.

Theoretical calculations

The optimized structures of the dinuclear salen-based indium complexes **XPOIn**, **XNOIn**, **XPCIn**, and **XNCIn** in the ground state (S_0) were determined using density functional theory (DFT) with the B3LYP functional[41] and 6-31G(d,p) levels.[42] The 6-31G(d,p) basis sets were used for atoms other than the central indium atoms. For indium atoms, the LANL2DZ effective core potential (ECP) and the corresponding basis set were used.[43] All electronic transition energies, including the electron correlations, were obtained from TD-DFT calculations using the hybrid B3LYP functional (TD-B3LYP).[44] All calculations were performed using the GAUSSIAN 16 program package.[45] The percentage contributions of the corresponding group in the complex to each molecular orbital were determined using the GaussSum 3.0 program.[46]

Conclusions

We developed a series of xanthene-anchored salen-based dinuclear indium complexes with well-defined open and closed topologies and systematically investigated the impact of dinuclear geometry on their structural and photophysical properties. The rigid yet non-planar xanthene linker enables controlled modulation of the relative orientation between the two salen–indium units without altering their primary coordination environments, thereby providing an ideal platform for isolating topology-dependent effects. Comprehensive photophysical analyses revealed a clear and consistent structure–property relationship. Although the closed dinuclear complexes exhibited more stabilized frontier molecular orbitals due to extended π-conjugation, they showed lower PLQYs than their open counterparts. This behavior originates from the reduced radiative decay rates and enhanced non-radiative relaxation pathways in the closed architectures, as supported by decay constant analysis and structural insights from single-crystal X-ray diffraction. These results indicate that excessive interchromophoric interactions, rather than promoting emission, can facilitate excited-state deactivation in dinuclear indium systems. This study highlights the key role of dinuclear topology in governing excited-state dynamics in salen–indium luminophores. By demonstrating that the controlled spatial separation of chromophoric units can be more effective than maximal conjugative coupling for enhancing emission efficiency, our results provide a clear framework for the rational design of multinuclear indium-based luminophores. This topology-oriented design concept can be broadly applied to the development of advanced main-group-metal luminescent materials.

Author contributions

Conceptualization and funding acquisition: M. H. Park; investigation: Y. Kim, J. H. Lee, H. Moon, and H. Mo; data curation: J. Lee and H. Hwang; writing – original draft: Y. Kim and J. H. Lee; writing – review & editing: Y. Kim, J. H. Park, and M. H. Park; and supervision: J. H. Park, Y. Kim, and M. H. Park.

Conflicts of interest

There are no conflicts to declare.

Data availability

The data supporting the findings of this study are included as part of the supplementary information (SI). Supplementary information: characterization data (^1H and ^{13}C NMR spectra) and X-ray crystallographic, spectroscopic, CV, and computational data for all indium complexes. See DOI: https://doi.org/10.1039/d6dt00428h.

CCDC 2530423 and 2530424 contain the supplementary crystallographic data for this paper.[47a,b]

Acknowledgements

This work was supported by the Chungbuk National University NUDP Program (2024) and the National Research Foundation of Korea (NRF), the Basic Science Research Program funded by the Ministry of Science and ICT (RS-2025-23523990 for M. H. Park and RS-2023-00248988 for J. H. Lee).

References

1 S. Ito, M. Gon, K. Tanaka and Y. Chujo, *Natl. Sci. Rev.*, 2021, **8**, nwab049.
2 Y. Aoyama, Y. Sakai, S. Ito and K. Tanaka, *Chem. – Eur. J.*, 2023, **29**, e202300654.
3 S. Ito, M. Gon and K. Tanaka, *Eur. J. Inorg. Chem.*, 2024, **27**, e202400180.
4 S. Ito, K. Tanaka and Y. Chujo, *Dalton Trans.*, 2024, **53**, 14858–14865.
5 H.-Y. Yin, J.-J. Gao, X. Chen, B. Ma, Z.-S. Yang, J. Tang, B.-W. Wang, T. Chen, C. Wang, S. Gao and J.-L. Zhang, *Angew. Chem., Int. Ed.*, 2020, **59**, 20147–20153.
6 P. Kaur and K. Singh, *J. Mater. Chem. C*, 2019, **7**, 11361–11405.
7 N. Boens, V. Leen and W. Dehaen, *Chem. Soc. Rev.*, 2012, **41**, 1130–1172.
8 Y. H. Lee, W. Lee, T. Lee, D. Lee, J. Jung, S. Yoo and M. H. Lee, *ACS Appl. Mater. Interfaces*, 2021, **13**, 45778–45788.

9 A. Kumar, H. Y. Shin, T. Lee, J. Jung, B. J. Jung and M. H. Lee, *Chem. – Eur. J.*, 2020, **26**, 16973–16801.
10 S. W. Kwak, H. Jin, J. H. Lee, H. Hwang, M. Kim, Y. Kim, Y. Chung, K. M. Lee and M. H. Park, *Inorg. Chem.*, 2019, **58**, 2454–2462.
11 S. W. Kwak, H. Jin, H. Shin, J. H. Lee, H. Hwang, J. Lee, M. Kim, Y. Chung, Y. Kim, K. M. Lee and M. H. Park, *Chem. Commun.*, 2018, **54**, 4712–4715.
12 S. W. Kwak, B. H. Choi, J. H. Lee, H. Hwang, J. Lee, H. Kwon, Y. Chung, K. M. Lee and M. H. Park, *Inorg. Chem.*, 2017, **56**, 6039–6043.
13 C. Sohn, J. Jeong, J. H. Lee, B. H. Choi, H. Hwang, G.-T. Bae, K. M. Lee and M. H. Park, *Dalton Trans.*, 2016, **45**, 5825–5832.
14 N. Lin, J. Qiao, L. Duan, J. Xue and L. Wang, *Chem. Mater.*, 2014, **26**, 3693–3700.
15 C. Pérez-Bolívar, S.-y. Takizawa, G. Nishimura, V. A. Montes and P. Anzenbacher Jr., *Chem. – Eur. J.*, 2011, **17**, 9076–9082.
16 S.-H. Liao, J.-R. Shiu, S.-W. Liu, S.-J. Yeh, Y.-H. Chen, C.-T. Chen, T. J. Chow and C.-I. Wu, *J. Am. Chem. Soc.*, 2009, **131**, 763–777.
17 S. Wang, *Coord. Chem. Rev.*, 2001, **215**, 79–98.
18 H. Mubarok, S. W. Kwak, J. H. Lee, H. Hwang, K. M. Lee, Y. Kim, M. H. Lee and M. H. Park, *Bull. Korean Chem. Soc.*, 2022, **43**, 1177–1183.
19 D. Xie, J. Jing, Y.-B. Cai, J. Tang, J.-J. Chen and J.-L. Zhang, *Chem. Sci.*, 2014, **5**, 2318–2327.
20 J. Jing, J.-J. Chen, Y. Hai, J. Zhan, P. Xu and J.-L. Zhang, *Chem. Sci.*, 2012, **3**, 3315–3320.
21 V. Béreau, C. Duhayon, A. Sournia-Saquet and J.-P. Sutter, *Inorg. Chem.*, 2012, **51**, 1309–1318.
22 V. Béreau, V. Jubéra, P. Arnaud, A. Kaiba, P. Guionneau and J.-P. Sutter, *Dalton Trans.*, 2010, **39**, 2070–2077.
23 K. Y. Hwang, H. Kim, Y. S. Lee, M. H. Lee and Y. Do, *Chem. – Eur. J.*, 2009, **15**, 6478–6487.
24 Y. Kim, J. Kim, J. H. Lee, H. Moon, H. Hwang, J. Lee, H. Kang, J. H. Park, Y. Kim and M. H. Park, *Bull. Korean Chem. Soc.*, 2025, **46**, 186–192.
25 Y. Kim, J. H. Lee, J. Kim, Y. Kim, H. Moon, H. Hwang, J. Lee, J. H. Park, Y. Kim and M. H. Park, *Bull. Korean Chem. Soc.*, 2024, **45**, 940–948.
26 Y. Kim, J. Kim, J. H. Lee, H. Moon, G. H. Noh, H. Hwang, J. Lee, J. H. Park, Y. Kim and M. H. Park, *Dalton Trans.*, 2023, **52**, 13379–13386.
27 S. W. Kwak, S. W. H. Mubarok, J. H. Lee, H. Hwang, K. M. Lee, M. H. Lee and M. H. Park, *Inorg. Chem. Front.*, 2022, **9**, 119–126.
28 C. H. Ryu, S. W. Kwak, H. W. Lee, J. H. Lee, H. Hwang, M. Kim, Y. Chung, Y. Kim, M. H. Park and K. M. Lee, *Inorg. Chem.*, 2019, **58**, 12358–12364.
29 S. W. Kwak, H. Kwon, J. H. Lee, H. Hwang, M. Kim, Y. Chung, Y. Kim, K. M. Lee and M. H. Park, *Dalton Trans.*, 2018, **47**, 5310–5317.
30 S. H. Lee, N. Shin, S. W. Kwak, K. Hyun, W. H. Woo, J. H. Lee, H. Hwang, M. Kim, J. Lee, Y. Kim, K. M. Lee and M. H. Park, *Inorg. Chem.*, 2017, **56**, 2621–2626.
31 S. W. Kwak, M. B. Kim, H. Shin, J. H. Lee, H. Hwang, J. Y. Ryu, J. Lee, M. Kim, Y. Chung, J. C. Choe, Y. Kim, K. M. Lee and M. H. Park, *Inorg. Chem.*, 2019, **58**, 8056–8063.
32 S. He, F. Wang, W.-L. Tong, S.-M. Yiu and M. C. W. Chan, *Chem. Commun.*, 2016, **52**, 1017–1020.
33 J. Rosenthal, T. D. Luckett, J. M. Hodgkiss and D. G. Nocera, *J. Am. Chem. Soc.*, 2006, **128**, 6546–6547.
34 J. Wang, Q. Dang, Y. Gong, Q. Liao, G. Song, Q. Li and Z. Li, *CCS Chem.*, 2021, **3**, 274–286.
35 J. Y. Yang, J. Bachmann and D. G. Nocera, *J. Org. Chem.*, 2006, **71**, 8706–8714.
36 D. A. Atwood, M. S. Hill, J. A. Jegier and D. Rutherford, *Organometallics*, 1997, **16**, 2659–2664.
37 S. Han, E. Yao, W. Qin, S. Zhang and Y. Ma, *Macromolecules*, 2012, **45**, 4054–4059.
38 W.-L. Tong, S.-M. Yiu and M. C. W. Chan, *Inorg. Chem.*, 2013, **52**, 7114–7124.
39 A. W. Kleij, D. M. Tooke, A. L. Spek and J. N. H. Reek, *Eur. J. Inorg. Chem.*, 2005, 4626–4634.
40 J. Shin, M. H. Lim and J. Han, *Bull. Korean Chem. Soc.*, 2024, **45**, 593–613.
41 P. J. Stephens, F. J. Devlin, C. F. Chabalowski and M. J. Frisch, *J. Phys. Chem.*, 1994, **98**, 11623–11627.
42 C. Lee, W. Yang and R. G. Parr, *Phys. Rev. B: Condens. Matter Mater. Phys.*, 1988, **37**, 785–789.
43 P. J. Hay and W. R. Wadt, *J. Chem. Phys.*, 1985, **82**, 270–283.
44 E. Runge and E. K. U. Gross, Density-functional theory for time-dependent systems, *Phys. Rev. Lett.*, 1984, **52**, 997–1000.
45 M. J. Frisch, G. W. Trucks, H. B. Schlegel, G. E. Scuseria, M. A. Robb, J. R. Cheeseman, G. Scalmani, V. Barone, G. A. Petersson, H. Nakatsuji, X. Li, M. Caricato, A. V. Marenich, J. Bloino, B. G. Janesko, R. Gomperts, B. Mennucci, H. P. Hratchian, J. V. Ortiz, A. F. Izmaylov, J. L. Sonnenberg, D. Williams-Young, F. Ding, F. Lipparini, F. Egidi, J. Goings, B. Peng, A. Petrone, T. Henderson, D. Ranasinghe, V. G. Zakrzewski, J. Gao, N. Rega, G. Zheng, W. Liang, M. Hada, M. Ehara, K. Toyota, R. Fukuda, J. Hasegawa, M. Ishida, T. Nakajima, Y. Honda, O. Kitao, H. Nakai, T. Vreven, K. Throssell, J. A. Montgomery Jr., J. E. Peralta, F. Ogliaro, M. J. Bearpark, J. J. Heyd, E. N. Brothers, K. N. Kudin, V. N. Staroverov, T. A. Keith, R. Kobayashi, J. Normand, K. Raghavachari, A. P. Rendell, J. C. Burant, S. S. Iyengar, J. Tomasi, M. Cossi, J. M. Millam, M. Klene, C. Adamo, R. Cammi, J. W. Ochterski, R. L. Martin, K. Morokuma, O. Farkas, J. B. Foresman and D. J. Fox, *Gaussian 16 Revision B.01*, Gaussian. Inc., Wallingford, CT, 2016.
46 N. M. O'Boyle, A. L. Tenderholt and K. M. Langner, A library for package independent computational chemistry algorithms, *J. Comput. Chem.*, 2008, **29**, 839–845.
47 (*a*) CCDC 2530423: Experimental Crystal Structure Determination, 2026, DOI: 10.5517/ccdc.csd.cc2qy3kc; (*b*) CCDC 2530424: Experimental Crystal Structure Determination, 2026, DOI: 10.5517/ccdc.csd.cc2qy3ld.

